Nuclear Instruments and Methods in Physics Research B 404 (2017) 74–80

Contents lists available at ScienceDirect

Nuclear Instruments and Methods in Physics Research B

journal homepage: www.elsevier.com/locate/nimb

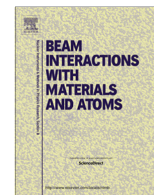


# Quadrupole lens alignment with improved STIM and secondary electron imaging for Proton Beam Writing

Sarfraz Qureshi [a], P. Santhana Raman [a,b], Alrik Stegmaier [c], Jeroen A. van Kan [a,*]

[a] Centre for Ion Beam Applications, Department of Physics, National University of Singapore, Singapore 117542, Singapore
[b] Department of Electrical and Computer Engineering, National University of Singapore, Singapore 117583, Singapore
[c] Physikalisches Institut, Georg-August-Universität Göttingen, 37077, Germany

ARTICLE INFO

*Article history:*
Received 2 September 2016
Received in revised form 5 November 2016
Accepted 5 December 2016
Available online 18 December 2016

*Keywords:*
Proton beam writing
STIM
Spectrum calibration
MCP detection efficiency
Quadrupole lens alignment
Automatic focusing

ABSTRACT

Minimal proximity effect coupled with uniform energy deposition in thin polymer layers make Proton Beam Writing (PBW) an intuitive direct-write lithographic technique. Feature sizes matching the focused beam spot size have been fabricated in photoresists down to 19 nm. Reproducible sub-10 nm beam focusing will make PBW a promising contender for sub-10 nm lithography. In this paper, we present beam size characterization by imaging a PBW resolution standard using transmitted/scattered ions and secondary electrons. Using Scanning Transmission Ion Microscopy (STIM) spectra for 1 and 2 MeV $H_2^+$ beams, we experimentally measure the thickness of the resolution standard to be 0.9 ± 0.1 μm, applying two independent calibration methods, which match the original intended thickness during fabrication. Through bias optimization of a Micro-Channel Plate (MCP), we show a tuneable secondary electron detection per proton for imaging with a maximum of 75% e/p for a beam of 1 MeV $H_2^+$. Based on STIM mode beam size measurement, we discuss considerations for quadrupole system alignment in order to remove higher order translational and rotational misalignments critical to achieve sub-40 nm spot sizes. A spot size of $13 \times 32$ nm$^2$ (STIM) was achieved using a newly developed interface, capable of autofocusing ion beams and performing PBW.

© 2016 Elsevier B.V. All rights reserved.

## 1. Introduction

MeV protons propagating through materials interact mostly by electronic scattering and a smaller fraction by end of the range nuclear scattering [1,2]. Protons, being relatively higher in mass than substrate electrons (≈1800:1), can travel in straighter paths leaving uniform energy loss trail [3,4]. Proton beams, focused to nanometer dimensions, have demonstrated fabrication of orthogonal, high aspect ratio structures in photoresist with low sidewall roughness [5–15]. Features down to 19 nm have been fabricated in HSQ using PBW technique [16] demonstrating that the ultimate feature size is limited only by the beam spot size. Nanostructures in HSQ ranging from 4 to 5 nm in width have been demonstrated using Electron Beam Lithography (EBL) [17] and Helium Ion Beam Lithography (HIBL) [18]. Four generations of free standing resolution standards (Ni grid) fabricated by PBW and subsequent electroplating [19–22] have enabled accurate beam size measurement from sub-micron dimensions down to sub-10 nm. A record spot size of $9.3 \times 32$ nm$^2$ was demonstrated for 2 MeV proton beam [23]. Reproducible sub-10 nm beam focusing coupled with minimal proximity effect will make PBW a promising contender for sub-10 nm lithography.

Next generation PBW at Centre for Ion Beam Applications (CIBA), NUS uses a spaced Oxford triplet quadrupole lens configuration to focus protons, attaining a demagnification of $857 \times 130$ [24] for ions accelerated by a 3.5 MV Singletron™ with an energy stability of 20 eV [25]. Beam focusing is performed by imaging a thin free standing resolution standard either by detecting transmitted/scattered ions or induced secondary electrons. In Scanning Transmission Ion Microscopy (STIM) [26], transmitted or scattered ions through the grid are collected by a silicon PIN diode positioned behind the grid in forward scattered direction. Direct beam and grid-scattered ions are differentiated in energy based on spectrum analysis. Subsequently, ON axis map or OFF axis maps could be generated resulting in improved image contrast. Beam size is extracted by fitting an error function to the line profile across two orthogonal edges of the grid [27].

In this paper, we describe a quadrupole lens alignment procedure based on improved STIM and secondary electron imaging, which enables sub-15 nm focusing in one direction for PBW. Using improved STIM setup and energy spectrum calibration by two

* Corresponding author.
*E-mail address:* phyjavk@nus.edu.sg (J.A. van Kan).

http://dx.doi.org/10.1016/j.nimb.2016.12.016
0168-583X/© 2016 Elsevier B.V. All rights reserved.

independent approaches, we experimentally measure the grid to be 0.9 ± 0.1 μm thick. However, STIM with the silicon PIN diode used in our system faces drawback due to detector damage leading to reduced count rate and poor energy resolution [28]. Besides detector resolution, reduced source brightness limits the total ion count while focusing the beam with smaller slit openings [29]. Imaging ion induced secondary electrons using a Micro-Channel Plate (MCP) in Chevron configuration partly alleviates this problem [30] by optimizing the applied bias which results in increased electron detection efficiency, we show a 75% secondary electron detection efficiency per proton measured for 1 MeV $H_2^+$ beam.

Misalignment of quadrupole lenses severely affects the beam focusing capability in the direction with lower demagnification. For a poorly aligned system, besides first order translational misalignment, higher order translational and rotational misalignment need to be removed to focus the beam below 100 nm [31]. Finally, we discuss the procedures adopted for quadrupole lens alignment aiming for smaller spot sizes. A newly developed PBW control interface capable of imaging, beam autofocusing, spectrum analysis and writing user defined patterns is also presented.

## 2. Experiments and results

### 2.1. Grid thickness measurement

Besides regular imaging, STIM can also be used for spectroscopic measurements [32,33]. Side-wall projection of the Ni grid [22] which can be calculated based on the grid thickness limits the reliability of beam size estimation. In order to experimentally determine the thickness of the PBW resolution grid [22], we calculate the energy loss of a molecular beam ($H_2^+$) through the Ni grid. This 1 MeV $H_2^+$ beam was scanned across an edge of the grid. As soon as the incoming high energy molecular hydrogen interacts with the surface of the grid bars, it splits into two protons each carrying half the energy. Each proton then propagates through the grid, losing energy mostly due to electronic scattering. Protons are then detected by a silicon PIN diode (Make: Hamamatsu, Model: S1223, with a detector resolution of 30 keV) positioned on-axis behind the grid. The beam was scanned across the edge of a grid bar and the corresponding STIM spectrum was recorded.

The energy of the direct or non-scattered beam corresponds to peak D in Fig. 1a. To determine the energy of the second peak, T in Fig. 1a, we performed a separate spectrum calibration (1 MeV $H_2^+$) scanning across Mylar foils of different thicknesses as shown in the inset of Fig. 1b (A = 0, B = 2.5 μm, and C = 5 μm), see Fig. 1b. Two smaller peaks labelled $B_p$ and $C_p$ correspond to the coincident or pile-up detection of two particles with energies corresponding to peaks B and C respectively.

Energy calibration was performed using pile up peak positions and estimated energy loss from SRIM [34] for Mylar. A similar exercise was repeated with a 2 MeV $H_2^+$ beam for Ni grid. Combining all the measured values, we estimate the Ni grid to be 0.9 ± 0.1 μm thick which corresponds to a 6.0 ± 0.6 nm side-wall projection, vital for achieving sub 10 nm beam focusing.

### 2.2. Dynamic secondary electron imaging

The ability to focus ion beams with a given demagnification is limited by the source brightness and system stability (thermal and mechanical) because of reduced count rate at smaller beam sizes [29]. Additionally, chromatic aberration of the beam, partially induced due to slit scattering, adds a halo to the beam spot in the image plane [35]. The transparency region in slits [35] was measured to be ~20 μm with no focusing action by quadrupole lenses [36]. However, in the active focusing, we observed a narrow transparency region (~1 μm) for molecular beams. Molecules dissociated through slit scattering are filtered out by the quadrupole lenses, thereby reducing the beam halo. At smaller slit openings, the ion count rate reduces to a few thousand ions per second. This increases the time to acquire the image, making it difficult to focus the beam with a 70% or higher goodness of fit. To alleviate this, an annular MCP in Chevron configuration [30] was installed in the end station [22]. Secondary electrons induced by ions hitting the grid bars are collected by the MCP connected to a pre-amplifier and counter.

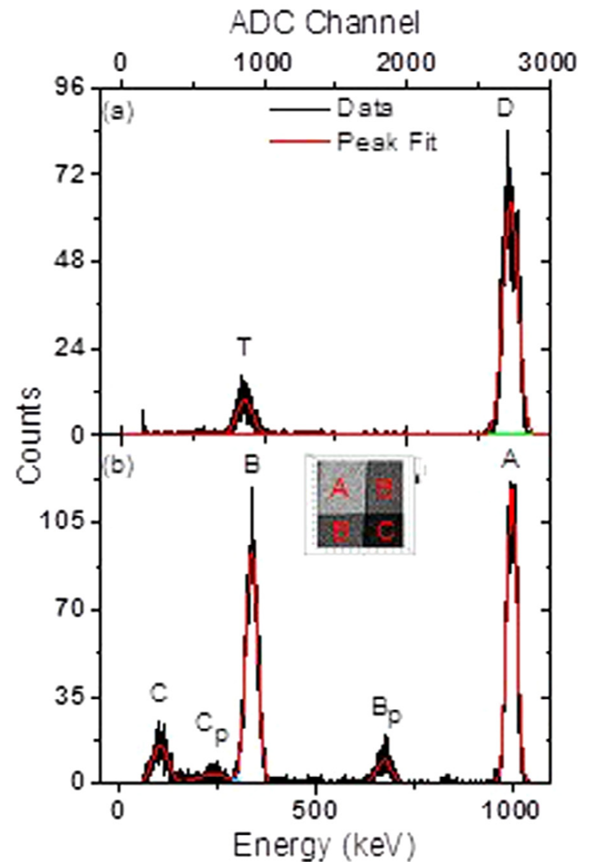


**Fig. 1.** (a) STIM Spectrum of 1 MeV $H_2^+$ through Ni grid. (b) STIM spectrum through 0, 2.5 μm and 5 μm thick layers of Mylar. Inset shows the ON-axis STIM image over a scan size of 130 × 130 μm².

Electron detection efficiency, defined as number of electrons reaching MCP collector per incident proton [37], of an MCP is highly sensitive to the bias voltage applied and the inter-plate acceleration voltage [30] (refer Fig. 2b inset for MCP schematics). It can be optimized by maximizing both the MCP gain (charge yield) and collection efficiency. MCP gain is optimized by varying the inter-plate voltage at fixed bias voltage to maximize the charge yield from the MCP plates. Collection efficiency can be optimized by comparing detection efficiency at variable bias voltage while keeping inter-plate voltage fixed. A 1 MeV $H_2^+$ beam was used to image the Ni grid with a molecular count rate of 3000 per second. Detection efficiency was then measured for three different back plate voltages: 2300 V, 2500 V and 2800 V at a fixed bias voltage of 100 V (see Fig. 2a for pulse height distributions). Detection efficiency increases as 16%, 42%, and 77% electrons per proton for the three back plate voltages respectively. Therefore, it can be concluded that increasing the inter-plate voltage at fixed bias voltage leads to increase in the MCP gain. Next, collection efficiency was compared for fixed inter-plate voltage values (2200 V and

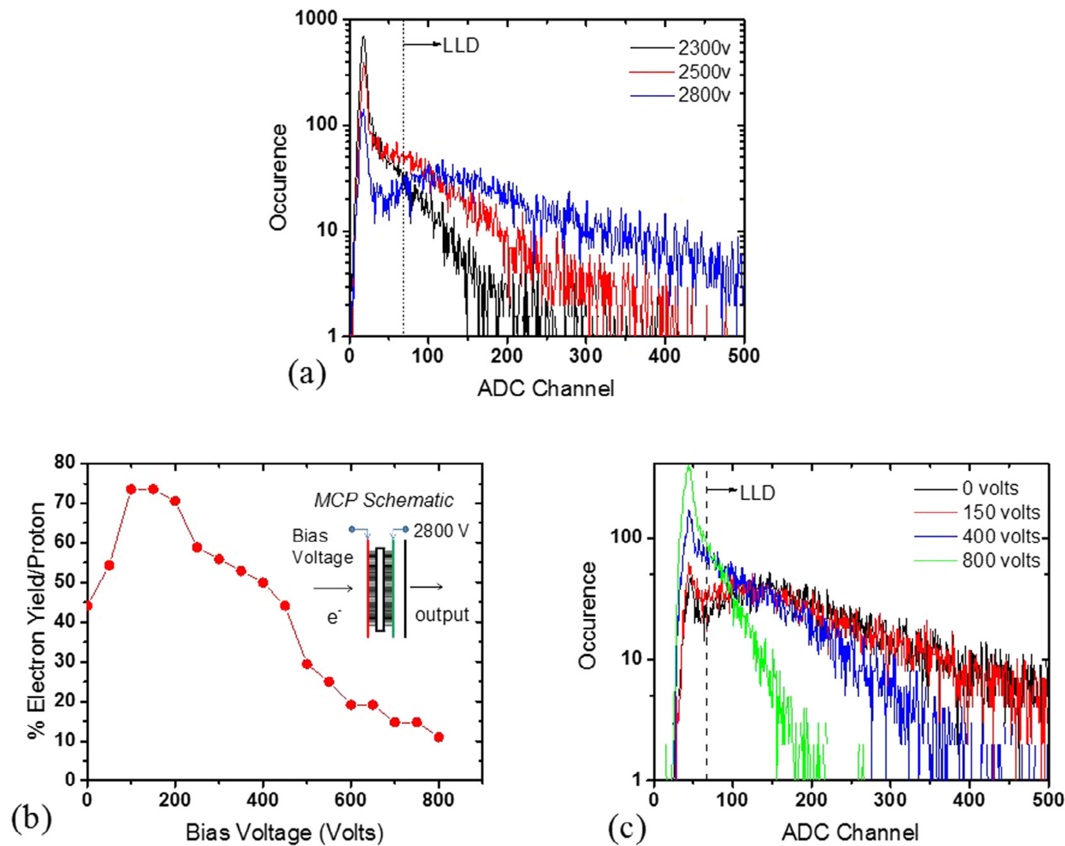


**Fig. 2.** (a) Pulse height distribution plotted for applied back plate voltages of 2300, 2500 and 2800 V at a fixed 100 V. (b) Variation of electron detection as a function of applied bias voltage to the MCP. Inset shows the MCP schematic in Chevron configuration. (c) Pulse height distribution plotted for applied biases of 0, 150, 400 and 800 V.

2400 V) to determine the contribution of changing bias voltage on detection efficiency (refer Table 1 for the plate voltages and detection efficiencies). A 19% increase was observed in the collection efficiency for both the cases when 2800 V was applied to the back plate keeping the inter-plate voltage constant at 2200 V and 2400 V. Thus, a 2800 V back plate potential leads to both optimum gain and collection efficiency.

In a separate experiment, MCP bias voltage to the front plate was varied from 0 to 800 V in steps of 50 V at a fixed back plate voltage of 2800 V to fine tune the detection efficiency. Fig. 2b shows the variation in secondary electron detection per proton, collected by the MCP as a function of bias voltage for 1 MeV $H_2^+$ beam with molecular count of 3400 per second. For an applied bias of 100–150 V, there is an enhancement in detection since more secondary electrons are attracted towards the front plate of the MCP. Further increasing the applied bias voltage, beyond 150 V, reduces the inter plate accelerating voltage, and thereby reducing the yield of secondary electrons within the micro channels. Pulse height distributions for the MCP pre-amplifier output is shown in Fig. 2c for different applied bias voltages at a fixed back plate voltage (2800 V). Integrating each curve starting from a Lower Level Discriminator (LLD) value, filtering out detector noise, results in the total electron yield at a particular applied bias voltage. This total count can be arranged in decreasing order for the applied bias of 150, 400, 0 and 800 V, corroborating the proportional decrease in secondary electron detection shown in Fig. 2b. Therefore, an optimal bias of 100–150 V at a back plate voltage of 2800 V results in improved [22] detection efficiency (75%) of secondary electrons per proton. Tuning the bias voltage of the MCP is also advantageous over STIM which is prone to detector damage at high count rates.

**Table 1**
Improvement in collection efficiency for variable bias voltages at fixed inter plate voltages.

| Bias voltage (V) | Back plate voltage (V) | Voltage across MCP (V) | Detection efficiency (e/p)% |
|---|---|---|---|
| 100 | 2300 | 2200 | 16 |
| 600 | 2800 | 2200 | 19 |
| 100 | 2500 | 2400 | 42 |
| 400 | 2800 | 2400 | 50 |

### 2.3. Quadrupole aberration correction

Rotational and/or translational misalignment of the quadrupole lens system for a spaced Oxford triplet configuration (refer Fig. 3h for schematic) can severely affect the otherwise achievable ultimate beam spot size [31]. First order translation misalignment can be checked by translating the collimator slits with respect to the optic axis of the quadrupoles. Fig. 3a shows the variation in beam full width half maximum (FWHM) in Y direction, measured using STIM as a function of collimator slit translations: $C_x$ and $C_y$ around the optic axis of the quadrupoles in X and Y directions respectively. With respect to Y FWHM, two notable characteristics indicating first order translational aberration are observed in Fig. 3a: system's inability to focus below 100 nm, and significant beam size variation with respect to the collimator slit position. However, X FWHM remains constant within measurement error as a function of collimator translation in X and Y directions (not shown). Collimator translation of 40 μm in $C_x$ and $C_y$ results in average X FWHM of 46 nm (±28) and 52 nm (±17) respectively. A

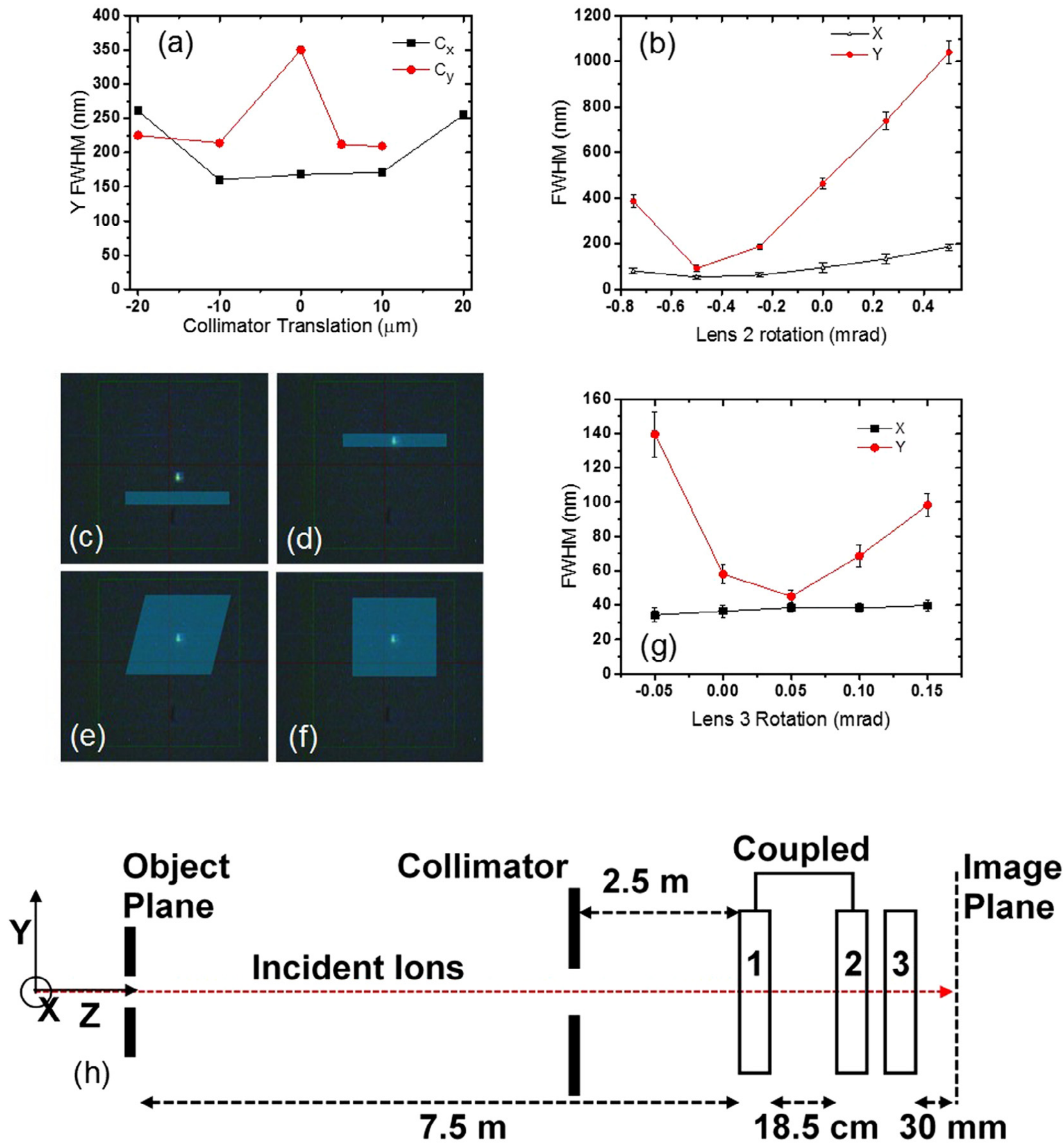


**Fig. 3.** (a) Y FWHM plotted as function of collimator translation ($C_x$ and $C_y$) in X and Y directions respectively around quadrupole optic axis. (b) Effect of lens 2 rotation upon beam size. Higher order translational aberration: (c) before and (d) after alignment. Higher order rotational aberration: (e) before and (f) after correction. (g) Fine tuning lens 3 rotation to correct for rotational misalignment. (h) System schematic.

well aligned system, on the other hand, shows no change in both X and Y FWHM, implying a corrected first order translation aberration. For the same object and collimator slit openings and 40 μm collimator translation, $C_x$, the X and Y FWHM remain constant within measurement error; 37 ± 9 nm and 75 ± 11 nm respectively. Similarly, for collimator translation $C_y$, we measure a constant X and Y FWHM of 33 ± 11 nm and 73 ± 12 nm respectively.

Due to diverging nature of lens 2, Y FWHM is prone to larger variation than X FWHM because of rotational misalignment as shown in Fig. 3b. Rotating lens 2 in a range of −0.75 to 0.5 mrad varies Y FWHM from 400 nm to 1 μm respectively with a minima at −0.5 mrad wherein Y FWHM drops to 90 nm without adjusting quadrupole excitation.

Fig. 3c–f shows a sequence of steps taken to align the quadrupole lenses using ion beam fluorescence from quartz thereby correcting higher order translation and rotational aberrations. A horizontal line focus is shown in Fig. 3c, which steers above and below the spot focus for under and over focusing respectively. This higher order translational aberration can only be corrected by translating lens 2 in +Y direction by 20 vm. Moving either lens 1 or 3 in ±Y didn't result in reduction of translational aberration, neither did moving the collimators in ±Y direction. Fig. 3d shows a corrected higher order translational aberration where the line focus doesn't steer away from the spot focus [31]. Fig. 3e shows higher order rotational misalignment which is corrected by rotating lenses 2 and 3 until a rectangular focus, as shown in Fig. 3f, is achieved. Following this alignment procedure, a beam focusing of $18 \times 32\ \text{nm}^2$ was attained for 2 MeV protons for an object slit opening of $8 \times 4\ \mu\text{m}^2$ and collimator slit opening of $30 \times 30\ \mu\text{m}^2$.

Next, with a beam size closer to the expected value, based on system demagnification in Y direction, a fine tuning of lenses 1 and 3 was carried out for rotational misalignment correction. Fig. 3g shows the variation of beam size as a function of rotation of lens 3. Over the range of rotation, a dip in Y FWHM is observed for a rotation of 0.05 mrad whereas X FWHM remains unperturbed. Rotating Lens 1 (not shown here) by −0.75 mrad to 0.25 mrad showed no effect on the beam spot size with beam FWHM remaining constant around $(43 \pm 10) \times (57 \pm 12)\ \text{nm}^2$.

Finally, for a 1 MeV $H_2^+$ beam, at a reduced brightness of 15 A/(m$^2$srV), Fig. 4a and b show STIM image and MCP image of the grid respectively. Extracted line scans in X and Y directions for STIM, shown in Fig. 4$a_x$ and $a_y$, results in a focused spot of 13 × 32 nm$^2$. Fig. 4$b_x$ and $b_y$ shows the corresponding X and Y extracted line scans for the secondary electron image acquired using MCP indicating a spot size of 15 × 35 nm$^2$. Both Fig. 4a and b were acquired in integration mode of 4 frames with 2048 pixel resolution for a scan size of 5 × 5 μm$^2$. To ensure 70% or above goodness of fit for the error function, neighbouring pixels were added to generate the line scans.

Fig. 5 shows the control interface written in LabVIEW 2011 [38] which is routinely used to image, autofocus and measure the beam spectrum. Besides controlling beam parameters, the interface is also used to write user defined patterns after a dose and scan size calibration. Two algorithms are employed for writing nano/microstructures: (1) Step and repeat, wherein the beam is scanned in a region defined by the input coordinates (limited to 130 × 130 μm$^2$ for 1 MeV protons) and the stage is stepped to the adjacent region to continue beam scanning. (2) Stage scan, wherein initial and final positions with a set velocity are defined within a total travel range of 20 mm and typical velocity of 1 μm/s for an optimized approach to fabricate smaller nanochannels [39,40]. Grid imaging, beam size measurements for STIM and MCP, and spectrum measurements described in this paper were performed by using this interface.

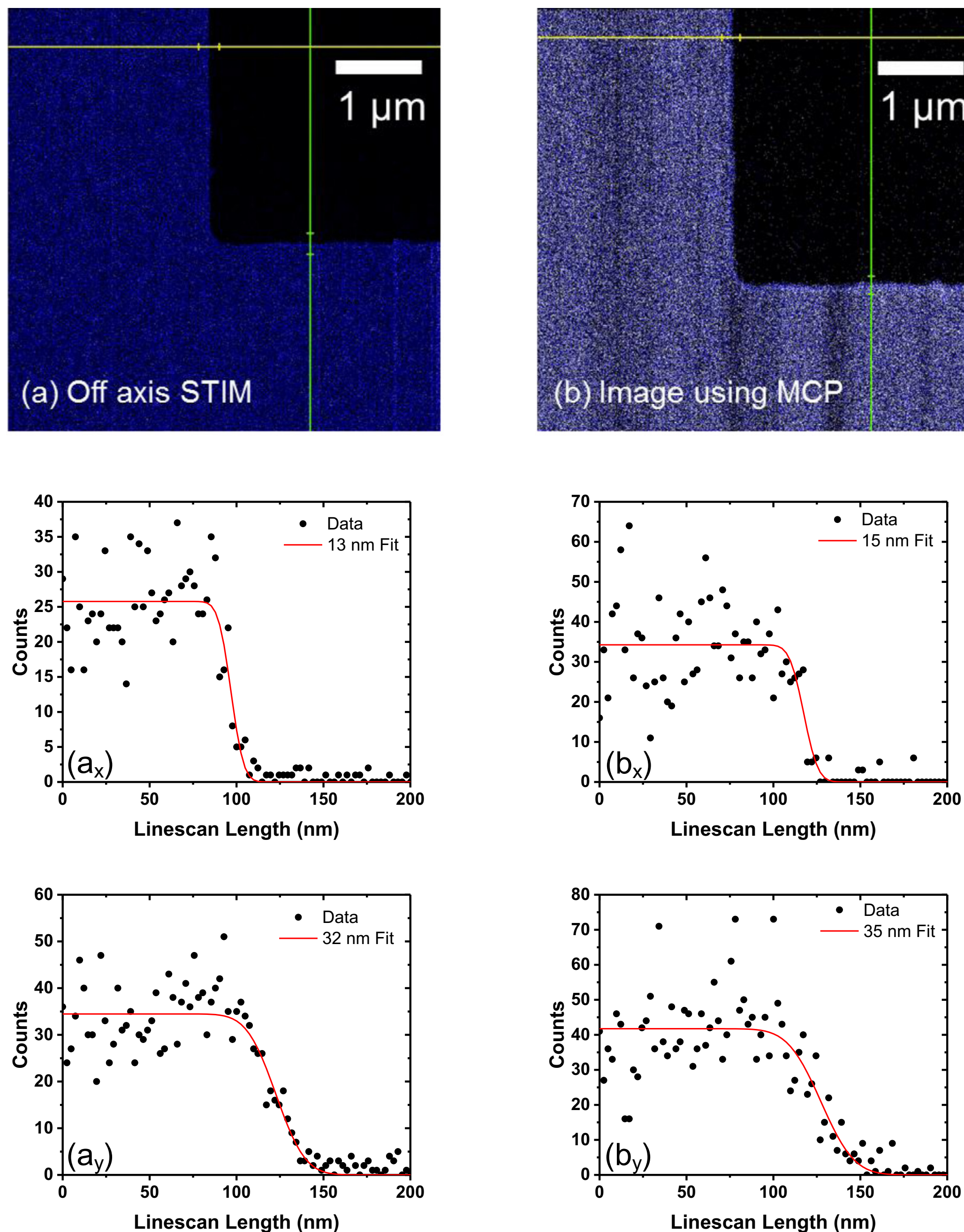


**Fig. 4.** Optimal focus after quadrupole alignment. (a) Off-axis scanning transmission ion microscopy images of the Ni resolution standard with ($a_x$, $a_y$) extracted line scans by adding 200 neighbouring pixels. (b) Secondary electron image acquired using MCP with ($b_x$, $b_y$) showing extracted line scans by adding 120 neighbouring pixels. Images (a) and (b) were taken with scan size of 5 × 5 μm$^2$.

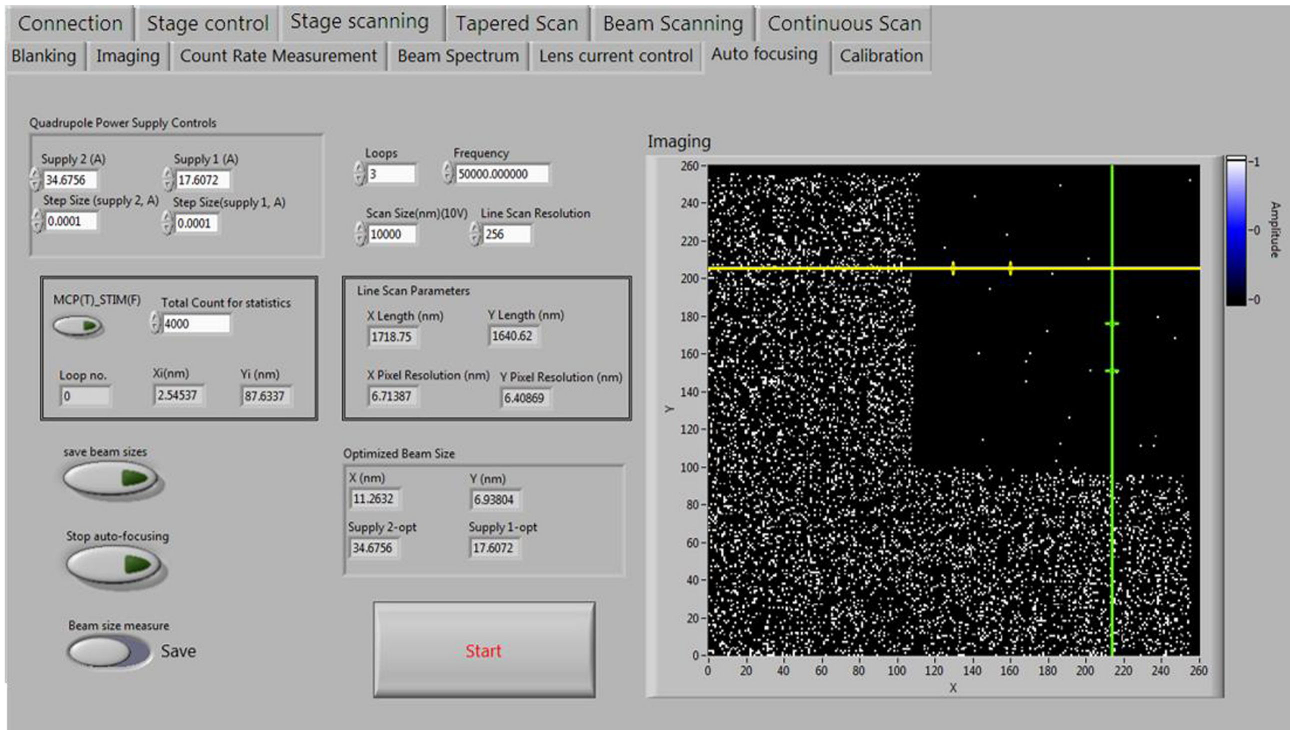


**Fig. 5.** Front panel of the PBW control interface used to image the resolution standard, autofocus beam spot and measure the spectrum. Also shown are the tabs that are routinely used to perform PBW using step and repeat or stage scanning.

## 3. Conclusion

Through an addition of STIM beam energy characterization we measured the thickness of the grid to be 0.9 ± 0.1 μm by coincidence particle approach and average energy loss estimated using SRIM simulations. The measured thickness corresponds to a side-wall projection of 6.0 ± 0.6 nm. Bias voltage optimization of MCP results in an improved secondary electron detection efficiency with a maximum detection of 75 secondary electrons per 100 protons for 1 MeV $H_2^+$. We also outlined a procedure for quadrupole lens alignment crucial for sub-40 nm spot sizes by correcting higher order translational and rotational aberrations. A focused spot size of $13 \times 32\ nm^2$ (using STIM) and $15 \times 35\ nm^2$ (using MCP) for 1 MeV $H_2^+$ at a reduced brightness of 15 A/($m^2$srV) was achieved. Brightness value of 42 A/($m^2$srV) has been observed, which when coupled with cleaner slits and further optimization will be crucial in achieving reproducible sub-10 nm focusing in one direction for PBW. Ongoing optimization at CIBA aims to achieve a reproducible sub-10 nm spot size for the fabrication of sub-10 nm structures [41]. Fabrication of resolution standard made with gold aimed at improving the yield of ion induced secondary electrons is underway. Coupled with the improved MCP detection efficiency, the approach will offer enhanced beam size estimation accuracy with higher statistics at lower acquisition timings. A high brightness source is under-development at CIBA [41], which when combined with higher order multipole lenses [42,43] will offer prospects of higher resolution and beam current density.

## References


[1] F. Watt, M.B.H. Breese, A.A. Bettiol, J.A. van Kan, Mater. Today 10 (2007) 20.
[2] F. Watt, Nucl. Instrum. Methods Phys. Res. Sect. B 158 (1999) 165.
[3] C.N.B. Udalagama, A.A. Bettiol, F. Watt, Nucl. Instrum. Methods Phys. Res. Sect. B 260 (2007) 384.
[4] C.N.B. Udalagama, A.A. Bettiol, F. Watt, Phys. Rev. B 80 (2009) 224107.
[5] J.A. van Kan, A.A. Bettiol, K. Ansari, F. Watt, Proc. SPIE 4343 (2001) 466.
[6] J.A. van Kan, A.A. Bettiol, F. Watt, Nucl. Instrum. Methods B 181 (2001) 258.
[7] H.J. Whitlow, M.L. Ng, V. Auzelyte, I. Maximov, L. Montelius, J.A. van Kan, A.A. Bettiol, F. Watt, Nanotechnology 15 (2004) 223.
[8] K. Ansari, J.A. van Kan, A.A. Bettiol, F. Watt, Appl. Phys. Lett. 85 (2004) 476.
[9] J.A. Van Kan, A.A. Bettiol, K. Ansari, E.J. Teo, T.C. Sum, F. Watt, Int. J. Nanotechnol. 1 (2004) 464.
[10] K. Ansari, P.G. Shao, J.A. van Kan, A.A. Bettiol, F. Watt, Nucl. Instrum. Methods Phys. Res. B 231 (2005) 407.
[11] S.Y. Chiam, J.A. van Kan, T. Osipowicz, C.N.B. Udalagama, F. Watt, Nucl. Instrum. Methods Phys. Res. B 260 (2007) 455.
[12] J.A. van Kan, A.A. Bettiol, F. Watt, Nucl. Instrum. Methods Phys. Res. B 260 (2007) 396.
[13] J.A. van Kan, P.G. Shao, K. Ansari, A.A. Bettiol, T. Osipowicz, F. Watt, Microsyst. Technol. 13 (2007) 431.
[14] W. Yue, S.Y. Chiam, Y. Ren, J.A. van Kan, T. Osipowicz, L. Jian, H.O. Moser, F. Watt, J. Micromech. Microeng. 18 (2008) 085010.
[15] J.A. van Kan, F. Zhang, S.Y. Chiam, T. Osipowicz, A.A. Bettiol, F. Watt, Microsyst. Technol. 14 (2008) 1343.
[16] Y. Yao, P.S. Raman, J.A. van Kan, Microsyst. Technol. 20 (2014) 2065.
[17] J.K.W. Yang, B. Cord, H. Duan, K.K. Berggren, J. Klingfus, S.W. Nam, K.B. Kim, M. J. Rooks, J. Vac. Sci. Technol., B 27 (2009) 2622.
[18] W.D. Li, W. Wu, R.S. Williams, J. Vac. Sci. Technol., B 30 (2012) 06F304.
[19] F. Watt, I. Rajta, J.A. van Kan, A.A. Bettiol, T. Osipowicz, Nucl. Instrum. Methods B 190 (2002) 306.
[20] J.A. van Kan, P.G. Shao, P. Molter, M. Saumer, A.A. Bettiol, T. Osipowicz, F. Watt, Nucl. Instrum. Methods Phys. Res. B 231 (2005) 170.
[21] F. Zhang, J.A. van Kan, S.Y. Chiam, F. Watt, Nucl. Instrum. Methods Phys. Res. B 260 (2007) 474.
[22] Y. Yao, M.W. van Mourik, P.S. Raman, J.A. van Kan, Nucl. Instrum. Methods Phys. Res. Sect. B 306 (2013) 265.
[23] Y. Yao, J.A. van Kan, Nucl. Instrum. Methods Phys. Res. Sect. B 348 (2015) 203.
[24] J.A. van Kan, P. Malar, A.B. de Vera, Rev. Sci. Instrum. 83 (2012) 02B902.
[25] D. Mous, R. Haitsma, T. Butz, R.H. Flagmeyer, D. Lehmann, J. Vogt, Nucl. Instrum. Methods Phys. Res. Sect. B 130 (1997) 31.
[26] G.S. Bench, G.J.F. Legge, Nucl. Instrum. Methods Phys. Res. B40/41 (1989) 655.
[27] C.N.B. Udalagama, A.A. Bettiol, J.A. van Kan, E.J. Teo, F. Watt, Nucl. Instrum. Methods Phys. Res. B 260 (2007) 390.
[28] R. Minqin, J.A. van Kan, A.A. Bettiol, L. Daina, C.Y. Gek, B.B. Huat, H.J. Whitlow, T. Osipowicz, F. Watt, Nucl. Instrum. Methods Phys. Res. B 260 (2007) 124.
[29] R. Szymanski, D.N. Jamieson, Nucl. Instrum. Methods Phys. Res. B 130 (1997) 50.
[30] J.L. Wiza, Nucl. Instrum. Methods 162 (1979) 587.
[31] G.W. Grime, F. Watt, Beam Optics of Quadrupole Probe-forming Systems, Adam Hilger Limited, 1984.
[32] R.M. Sealock, D.N. Jamieson, G.J.F. Legge, Nucl. Instrum. Methods Phys. Res. B29 (1987) 557.

[33] M. Cholewa, G.J.F. Legge, Nucl. Instrum. Methods Phys. Res. B 54 (1991) 109.
[34] J.F. Ziegler, J.P. Biersack, U. Littmark, The Stopping and Range of Ions in Solids, Pergamon, New York, 1985, Available from: <http://www.srim.org>.
[35] F. Watt, T.F. Choo, K.K. Lee, T. Osipowicz, I. Orlic, S.M. Tang, Nucl. Instrum. Methods B 104 (1995) 101.
[36] J.A. van Kan, P. Malar, A.B. de Vera, C. Xiao, A.A. Bettiol, F. Watt, Nucl. Instrum. Methods Phys. Res. A 645 (2011) 113.
[37] E. Veje, Nucl. Instrum. Methods 194 (1982) 433.
[38] http://www.ni.com/labview/release-archive/2011/.
[39] C. Zhang, K. Jiang, F. Liu, P.S. Doyle, J.A. van Kan, J.R.C. van der Maarlel, LOC 13 (2013) 2821.
[40] J.A. van Kan, C. Zhang, P. Malar, J.R.C. van der Maarel, Biomicrofluidics 6 (2012), 036502-1.
[41] N. Liu, X. Xu, R. Pang, P.S. Raman, A. Khursheed, J.A. van Kan, Rev. Sci. Instrum. 87 (2016) 02A903.
[42] G. Hinderer, G. Dollinger, G. Datzmann, H.J. Kiirner, Nucl. Instrum. Methods Phys. Res. B 130 (1997) 51.
[43] G. Datzmann, G. Dollinger, G. Hinderer, H.J. Korner, Nucl. Instrum. Methods Phys. Res. B 158 (1999) 74.